
XIEFF REPRESENTATION FOR NEAR-FIELD OPTICS

Anonymous authors

Paper under double-blind review

ABSTRACT

Near-field optics, or near-field electrodynamics, is a field that studies the interaction between materials and light at spatial scales smaller than the wavelength. At these extremely small scales, below the diffraction limit, the interaction between materials and electromagnetic fields can exhibit unique behaviors and properties not observed in conventional optics. This area of research is crucial for understanding the optical characteristics of nanotechnical systems and nanoscale biological objects. One of the primary tools used in near-field optics research is scanning near-field optical microscopy (SNOM), which allows researchers to measure near-field optical images (NFI). However, these images often lack visual clarity and interpretability, hindering a comprehensive understanding of the properties of the probed particles.

The main goal of this paper is to introduce a novel approach that addresses these challenges. Inspired by the progress in physics-informed neural networks (PINNs) and its applied subdomain physics-informed computer vision (PICV), we propose an unsupervised method that introduces the XiEff representation – a neural field-based parameterization of the effective susceptibility tensor. By integrating XiEff into the Lippmann-Schwinger integral equation framework for near-field optics, we develop an optimization strategy to reconstruct the effective susceptibility distribution directly from NFI data.

The optimized XiEff representation provides an interpretable and explainable model of the particle’s shape. Extensive evaluations on a synthetically generated NFI dataset demonstrate the effectiveness of the method, achieving high intersection-over-union scores between XiEff and ground truth shapes, even for complex geometries. Furthermore, the approach exhibits desirable robustness to measurement noise, a crucial property for practical applications. The XiEff representation, combined with the proposed optimization framework, potentially introduces a valuable tool for enabling explainable near-field optics imaging and enhancing the understanding of particle characteristics through interpretable representations

1 INTRODUCTION

Near-field optics Girard & Dereux (1996) is a branch of optical physics that explores the behavior of light at scales smaller than the diffraction limit of conventional optics, where unique optical phenomena arise due to near-field interactions. Scanning near-field optical microscopy Durig et al. (1986) (SNOM) is a powerful technique that employs a nanoscopic probe to measure near-field optical signals with exceptional spatial resolution, providing unprecedented access to optical properties at the nanoscale.

Despite SNOM’s advanced capabilities, the raw near-field images (NFIs) it produces often lack visual clarity and interpretability, making it challenging to infer the physical properties and geometry of the probed particles. This limitation hinders a comprehensive understanding of near-field optical interactions and restricts the potential applications of SNOM.

To address this challenge, we propose a novel approach that introduces the XiEff representation — a neural field-based parameterization Xie et al. (2022) of the effective susceptibility tensor \hat{X} Lozovski (2010). Our method leverages recent advancements in Physics-Informed Neural Networks (PINNs) Raissi et al. (2019) and their applied subdomain, Physics-Informed Computer Vision

(PICV) Banerjee et al. (2024). PINNs integrate physical laws into neural network training by embedding partial differential equations (PDEs) and boundary conditions into the loss functions, guiding the learning process with physics-based constraints. PICV extends these principles to computer vision tasks.

Neural Radiance Fields (NeRFs) Mildenhall et al. (2021), which are a part of PICV, have revolutionized 3D reconstruction and novel view synthesis by representing scenes as neural networks. In our work, we adopt similar concepts but focus on representing the effective susceptibility tensor as neural fields tailored for near-field optics.

We integrate the XiEff representation into the Lippmann-Schwinger integral equation Girard et al. (1995) framework, which utilizes Green’s functions to describe electromagnetic field interactions. This approach allows us to incorporate physical laws directly into our neural network without relying explicitly on PDEs or boundary conditions, making it suitable for practical problems where such information may be inaccurate or unknown.

The main contributions of this work are:

1. **Novel Computer Vision Algorithm** We introduce the XiEff representation, a new computer vision algorithm that uses neural fields to model the effective susceptibility tensor in near-field optics imaging. Our method reconstructs the effective susceptibility XiEff directly from near-field imaging data. This representation provides an interpretable model connected to the optical characteristics of the object. It offers meaningful physical insights that align with human perception, making the object’s optical characteristics understandable, unlike the raw near-field images that are hard to interpret.
2. **Successful Validation** Our method was validated through extensive synthetic data experiments. The XiEff representation achieved high IoU scores with particles shapes, showed robustness to noise, and was computationally efficient and hyperparameters free. It successfully reconstructs simple and complex particle shapes, maintaining reliable convergence without requiring labeled data or external data.
3. **SNOM Scanning Strategy** We propose a SNOM scanning method using randomly varied external fields to enhance data diversity, leading to more accurate reconstructions. This strategy is potentially universal, capable of improving various inverse algorithms in similar domains.
4. **Benchmark Dataset** We created a comprehensive dataset of particle shapes and their NFIs, to be released as the first benchmark for inverse problems in near-field optics and PINNs

In summary, we aim to expand computer vision into the new modality of near-field optics by enhancing interpretability and effectiveness of near-field imaging.

2 RELATED WORK

Physics-informed neural networks (PINNs) have emerged as a powerful framework for solving complex physical systems by incorporating physical laws, typically in the form of partial differential equations (PDEs), into neural network loss functions Raissi et al. (2019). While PINNs have shown remarkable success across various domains, comprehensive surveys Huang et al. (2022); Banerjee et al. (2024); Wang et al. (2024b;a) indicate that their applications have primarily focused on PDEs, despite many physical systems having correspondents integral formulations. The integration of integral equations within the PINNs framework remains relatively unexplored, with only a few theoretical studies addressing this approach Sun et al. (2023).

An applied extension of PINNs, Physics-Informed Computer Vision (PICV) Banerjee et al. (2024), has successfully incorporated physical laws into computer vision algorithms. Our work on near-field imaging extends the PICV paradigm by integrating electromagnetic theory into computer vision algorithm to enable interpretable reconstruction of particle characteristics from SNOM measurements. Like other PICV applications, our work confronts several key challenges common in PICV Banerjee et al. (2024), including balancing physics and data constraints, selecting appropriate physics priors, developing standardized datasets and benchmarks, computational efficiency, and maintaining interpretability and explainability.

108 In the context of near-field problems, the conventional approach involves Maxwell’s equations,
109 which comprise four fundamental equations and up to six boundary conditions Jackson (2012).
110 When implementing these within PINNs, significant challenges arise in loss function balancing
111 Wang et al. (2021) and handling boundary conditions, particularly in inverse problems where the
112 target shape needs to be reconstructed. The Lippmann-Schwinger (LS) equation offers an attrac-
113 tive alternative for such inverse problems, as it inherently handles boundary conditions through its
114 integral formulation.

115 Recent works in near-field optics has demonstrated the application of PINNs based on full-vector
116 Maxwell’s PDEs for solving inverse problems Chen et al. (2020); Chen & Dal Negro (2022). The
117 first approach Chen et al. (2020) enabled the inverse retrieval of scalar photonic nanostructure proper-
118 ties, such as electric permittivity and magnetic permeability, from near-field data. Subsequently, the
119 second approach Chen & Dal Negro (2022) reconstructed spatial material characteristics of a spher-
120 ical object. However, this experiment relied on measurements of the field distribution directly near
121 the object’s surface (which shape’s mirrored the particle’s shape), and required substantial computa-
122 tional resources (10 hours on a 1080Ti GPU, 50×50×30 computational grid). Both research efforts
123 were constrained to investigating objects with very simple geometries in 2D case, and for 3D case
124 inverse problem reported only single experiment with spherical object.

125 A notable example of applying PINNs in the domain of diffraction tomography is the work Saba
126 et al. (2022). In this work, a UNet-based physics-informed neural network is used as a forward
127 solver, trained on a synthetic dataset of biological cell objects. The forward solver is then employed
128 in an inverse reconstruction of the refractive index (RI) by minimizing the discrepancy between
129 predicted and measured scattered fields. Despite being trained mainly on synthetic data, this method
130 demonstrates good performance on real datasets. However, a limitation of this approach is that it
131 performs best for object geometries similar to those present in the synthetic dataset. The proposed
132 method also shows good computational efficiency (4.5 min, 64×64×64 computational grid).

133 In the radio frequency domain Zhang et al. (2024) utilized the integral Lippmann-Schwinger equa-
134 tion with PINNs for modeling electromagnetic scattering in complex 2D shapes. However, their
135 focus remained on forward problem solving rather than inverse problems.

136 Neural Radiance Fields (NeRF) Xie et al. (2022) have achieved remarkable success in computer
137 vision and scene rendering. Interestingly, NeRF can be interpreted as an integral equation where
138 boundary conditions are explicitly encoded, effectively serving as a phenomenological physical
139 model. However, NeRF’s novel view interpolations often exhibit visual inconsistencies and geomet-
140 ric roughness. Recent research aims to address this ”generalization gap” by incorporating physical
141 principles rather than relying solely on simple phenomenological model Li et al. (2023).

142 The limited exploration of integral equations in physics-informed machine learning presents an op-
143 portunity for innovation. Integral formulations often offer advantages in handling boundary condi-
144 tions and provide more natural representations for certain physical phenomena than decomposition
145 physical laws into differential equations, boundary conditions and initial conditions. This untapped
146 potential suggests promising directions for future research, particularly in problems both theoretical
147 and applied PINNs.

150 3 THE LIPPMANN-SCHWINGER EQUATION

151
152
153 The problem under consideration can be described as follows. We consider an external electric field
154 and a homogeneous dielectric that interacts with the field. The dielectric undergoes polarization
155 thus creating an induced electric field. Any measuring device outside the dielectric will measure
156 superposition \vec{E} of the initial external field $\vec{E}^{(0)}$ and polarization field \vec{E}^{pol} (see figure 1). We will
157 try to recover the form of the dielectric basing on the measurements performed at some distance
158 from it.

159 As a first step we need to express the problem in an analytical way. It is well-known that such
160 matter-field interactions are governed by the Maxwell’s equations. But the latter ones are unwieldy,
161 thus we will use the fact that for a homogeneous, linear, non-dispersive, non-magnetic dielectric
in an external field, the four Maxwell’s equations can be transformed into the Lippman-Schwinger

162
163
164
165
166
167
168
169
170
171
172
173
174
175
176
177
178
179
180
181
182
183
184
185
186
187
188
189
190
191
192
193
194
195
196
197
198
199
200
201
202
203
204
205
206
207
208
209
210
211
212
213
214
215

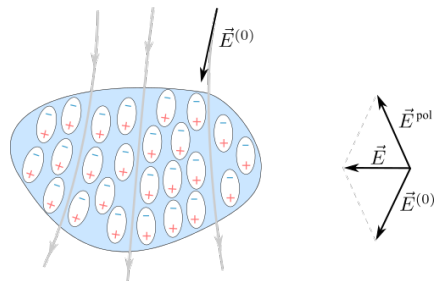


Figure 1: Measurement is performed outside the particle

equation (LS) Girard et al. (1995)

$$\vec{E}(\vec{r}, \omega) = \vec{E}^{(0)}(\vec{r}, \omega) - \iint\int_{\mathbb{R}^3} \hat{\mathcal{G}}(\vec{r}, \vec{r}', \omega) \hat{\chi}(\vec{r}', \omega) \vec{E}(\vec{r}', \omega) d\vec{r}' \quad (1)$$

where $\hat{\chi}$ is the local electric susceptibility and $\hat{\mathcal{G}}$ is a dyadic propagator described by a complicated formula

$$\hat{\mathcal{G}} = \left(\frac{4\pi\omega^2}{c^2} \mathbb{I} + \vec{\nabla} \otimes \vec{\nabla} \right) \frac{e^{i\omega|\vec{r}-\vec{r}'|/c}}{|\vec{r}-\vec{r}'|}. \quad (2)$$

It is supposed here that the field may be varying with angular frequency ω and c is the speed of light. Please note that for vacuum $\hat{\chi} = 0$, thus integration is effectively performed over the volume of the particle only.

For our purposes we suppose that the external field is slowly varying $\omega \rightarrow 0$ (so-called near-field approximation that applies to a scanning near-field optical microscopy (SNOM) probe and many other cases), thus (1) and (2) can be simplified and rewritten in Cartesian coordinates in a component-wise form

$$E_i(\vec{r}) = E_i^{(0)}(\vec{r}) - \iint\int_{\mathbb{R}^3} \mathcal{G}_{ij}(\vec{r}, \vec{r}') \chi_{jk}(\vec{r}') E_k(\vec{r}') d\vec{r}' \quad (3a)$$

$$\mathcal{G}_{ij} = \frac{\partial^2}{\partial x_i \partial x_j} \frac{1}{|\vec{r} - \vec{r}'|}. \quad (3b)$$

The undisturbed external field $\vec{E}^{(0)}$ is supposed to be known everywhere, while the actual electric field \vec{E} is known only starting at some distance outside the particle (i.e. we cannot measure inside the particle, neither do we know the form of the particle to measure the field at the boundary).

4 EFFECTIVE SUSCEPTIBILITY

Now the problem boils down to the continuation of \vec{E} from the areas it was measured to the whole space. This is a non-trivial task not only due to the complexity of (3), but the fact that $\hat{\chi}$ is unknown as well: if we knew it, we would easily recover the shape of the particle due to the fact that $\hat{\chi} = 0$ for vacuum but not for the particle. To tackle the problem we are using the effective susceptibility Lozovski (2010)

$$X_{jk} = \chi_{jk} \frac{E_k^{(0)}}{E_k}.$$

Please note that in this case no summation over repeating indices is performed.

Now the final form of the LS equation can be written as

$$E_i(\vec{r}) = E_i^{(0)}(\vec{r}) - \iint\int_{\mathbb{R}^3} \mathcal{G}_{ij}(\vec{r}, \vec{r}') X_{jk}(\vec{r}') E_k^{(0)}(\vec{r}') d\vec{r}'. \quad (4)$$

Here the only unknown quantity is the X , as the \vec{E} in the left-hand side of the formula is measured outside the particle, for example via SNOM probe, thus known.

In computational physics, several methodologies exist for solving the LS equation (3). The Discretization Paulus & Martin (2001) and Iteration Methods Martin et al. (1994) are traditional methods that are computationally hard and do not handle resonance effectively. The Diagram Method is a semi-analytical approach that uses effective susceptibility abstraction, simplifying computation to a quadrature process. It performs well under resonant conditions and is best suited for shapes with known analytical solutions Bozhevolnyi et al. (2001).

In the next section, we reuse the effective susceptibility concept with PINN paradigm and low computational cost for inference (4) will make inverse modeling efficient.

4.1 METHOD

In our method, we employ a neural field to mimic the effective susceptibility tensor $\hat{X}(\mathbf{r})$. This approach is akin to the principles of Physics-Informed Neural Networks (PINNs), where physical laws guide the training of neural networks. Instead of incorporating partial differential equations and boundary conditions explicitly and use excess hyperparameters Chen et al. (2020); Chen & Dal Negro (2022), we integrate the neural representation of the effective susceptibility tensor into the Lippmann-Schwinger equation. As result proposed algorithms is hyperparameters free and is more efficient in tuning. This allows the network to learn a physically consistent representation of the susceptibility tensor directly from NFI data.

The tensor $\hat{X}(\vec{r})$, which is a 3×3 tensor in three-dimensional space (or 2×2 in two-dimensional cases), is parameterized as a neural network function $\hat{X}(\vec{r}) = \text{XiEff}(\vec{r}, \Theta)$ with parameters Θ . With this representation we can reformulate the Lippmann-Schwinger equation (4) by simply setting $X_{ij}(\vec{r}) \rightarrow \text{XiEff}_{ij}(\vec{r}, \Theta)$. Now field \vec{E} can be treated as depending from Θ through XiEff via the equation (4), thus we write $\vec{E}(\vec{r}; \text{XiEff}(\vec{r}; \Theta))$, or $\vec{E}(\vec{r}; \Theta)$ for short.

Measuring the electric field by physical device, say SNOM probe Durig et al. (1986), we can say that at the points \vec{r}_i its value should constitute $\vec{E}_i^{(obs)}$, thus the loss function is expected to be

$$\mathcal{L}(\Theta) = \sum_{i=1}^N \|\vec{E}(\vec{r}_i; \Theta) - \vec{E}_i^{(obs)}\|^2 + \lambda \mathcal{L}_{\text{reg}}(\Theta). \quad (5)$$

We expect that after optimization the neural network function $\text{XiEff}(\vec{r}, \Theta)$ which represents the effective susceptibility will approach zero in regions outside the object to align with real-world data: the susceptibility of vacuum is zero. Thus we impose regularization in form of

$$\mathcal{L}_{\text{reg}}(\Theta) = \sum_{i=1}^N \|\text{XiEff}(\vec{r}_i, \Theta)\|, \quad (6)$$

where λ signifies the regularization strength. This part of loss is optional.

The minimization of the loss function $\mathcal{L}(\Theta)$ is achieved through gradient-based optimization algorithms, such as stochastic gradient descent (SGD). The ultimate expectation is that the morphology of the optimized $\text{XiEff}_{ij}(\vec{r}; \Theta)$ will resemble the form of the physical particle, thereby providing a mechanism for surface reconstruction within the domain of near-field optical imaging and similar setups.

Before we move to the description of experiments, one more concern should be addressed. We want to be sure that the results will be reliable, i.e. they do not change significantly due to a small variation in the input data. This is crucial when working with physical measurements, as every real-world device provides measurement with certain level of noise. Thus we prove:

Lemma. If the observed electric field $\vec{E}_i^{(obs)}$ is perturbed by noise $\vec{\xi}$ with a mean of zero $\mathbb{E}[\vec{\xi}] = 0$, the gradient $\vec{\nabla}_{\Theta} \mathcal{L}(\Theta)$ of the loss function (5) with regularization (6) remains unbiased.

270
271
272
273
274
275
276
277
278
279
280
281
282
283
284
285
286
287
288
289
290
291
292
293
294
295
296
297
298
299
300
301
302
303
304
305
306
307
308
309
310
311
312
313
314
315
316
317
318
319
320
321
322
323

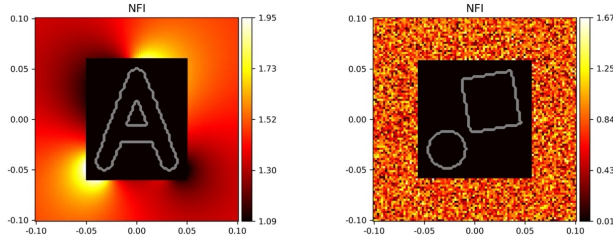


Figure 2: Example of the dataset images without (left) and with (right) random component to the pumping SNOM field. Hidden shape is overlaid for demonstration purposes only and not accessible by NN.

◀ Consider the derivative of the $\vec{\nabla}_{\Theta} \mathcal{L}(\Theta)$ from (5). The norm squared has form $\vec{x}^T \vec{x}$, thus we can use equality from Petersen et al. (2008) to get

$$\vec{\nabla}_{\Theta} \mathcal{L}(\Theta) = 2 \sum_{i=1}^N \left(\vec{E}(\vec{r}_i; \Theta) - \vec{E}_i^{(obs)} \right) \cdot \vec{\nabla}_{\Theta} \vec{E}(\vec{r}_i; \Theta) + \lambda \vec{\nabla}_{\Theta} \mathcal{L}_{reg}(\Theta).$$

We can get $\vec{\nabla}_{\Theta} \mathcal{L}^{(noisy)}(\Theta)$ by simply changing $\vec{E}_i^{(obs)} \rightarrow \vec{E}_i^{(obs)} + \vec{\xi}_i$, thus mean of the difference

$$\vec{\nabla}_{\Theta} \mathcal{L} - \mathbb{E}[\vec{\nabla}_{\Theta} \mathcal{L}^{(noisy)}] = 2 \sum_{i=1}^N \mathbb{E}[\vec{\xi}_i] \cdot \vec{\nabla}_{\Theta} \vec{E}(\vec{r}_i; \Theta),$$

where we used the linearity of mean to simplify the expression. Now recall that $\mathbb{E}[\vec{\xi}] = 0$ by assumption, thus mean of the difference is zero that concludes the proof. ■

This simplification shows that the gradient of the loss function with respect to the network parameters Θ remains unbiased in the presence of noise. Consequently, the optimization via gradient descent is robust, converging to a solution that is not skewed by the noise in the observed data. This robustness is essential for ensuring the reliability of the optimization process in practical applications where measurement noise is inevitable.

5 DATASET

In this study, we focus on 2D geometric cases because generating real-world NFI data requires creating nanosized particles with diverse shapes and measuring them, which is a lengthy and costly process. Instead, we chose to create a synthetic 2D dataset, as it is easier to visualize, provides diverse shapes, and typically, NFI images measured by SNOM are also usually 2D, making the research process more efficient. This can be understood as either considering a 2D slice of the system or as a projection of a system that extends infinitely along the Z axis.

We have developed a synthetic dataset, herein referred to as the dataset, consisting of various particles alongside their corresponding calculated near-field images (NFIs). A typical visualization of our dataset you can find at Figure 2. The particle’s shape is obscured by an object mask — essentially a rectangular mask that covers the particle with padding — depriving the neural network of any information about the particle’s form (previous work Chen & Dal Negro (2022) relied on measurements taken directly near the surface, which resulted in unintended leakage of the object’s form due to the measurement method). The corresponding NFI is calculated according to LS solution outside the object mask thus can be measured in a real-life experiment with SNOM probe or other method. Both the X and Y coordinates are normalized to the wavelength, ensuring all NFIs within the range of -0.1 to 0.1 . The observed field (NFI), $\vec{E}^{(obs)}$ is also presented in normalized units.

For the initial dataset (see Fig. 2) of near-field images, the external field (e.g. pumping field of SNOM Durig et al. (1986)) is kept constant at $\vec{E}^{(0)} = (1; 1; 0)$. The dataset encompasses a total of 121 images, including a set of randomly generated simple shapes (17 ellipses, 22 rectangles, 12

324
325
326
327
328
329
330
331
332
333
334
335
336
337
338
339
340
341
342
343
344
345
346
347
348
349
350
351
352
353
354
355
356
357
358
359
360
361
362
363
364
365
366
367
368
369
370
371
372
373
374
375
376
377

Table 1: IoU metrics for different shape categories and dataset variants.

Dataset	Ellipse	Rectangle	Convex	Union	Character	Avg
constant	93.51	84.08	77.02	78.65	61.70	76.72
random	93.75	89.85	84.89	81.01	66.59	80.79

convex polygons) and more complex forms (36 characters spanning 0-9, A-Z, and 31 union pairs of simple shapes). The susceptibility of the particles was randomly selected from a range of 0.5 to 1.5 and set diagonal and equal for all components. This choice of isotropic susceptibility is well-justified as most common dielectric materials exhibit only weak anisotropic responses at optical frequencies Landau et al. (2013); Boyd et al. (2008). For our 2D geometry, where system symmetry further supports such treatment, this approximation maintains physical relevance while keeping the inverse problem tractable. All scripts involved in generating the dataset and implementing the proposed solution will be made accessible on GitHub.

Additionally, we have developed a second variation of the dataset that utilizes the same shapes and susceptibility but incorporates an external field $\vec{E}^{(0)}$ (pumping field of SNOM is controlled parameter of experiment) that, unlike the previous case, is randomized for each individual SNOM probe position. This approach simulates an ensemble of measurements under varying field conditions, with $\vec{E}^{(0)}$ sampled from a uniform distribution on the square $[-1; 1] \times [-1; 1] \times 0$ for every data point measurement. While this dataset of NFIs may lack some visual clarity, it offers several benefits for the XiEff representation optimization. It enhances optimization robustness by exposing the model to diverse field conditions, helps prevent overfitting to specific configurations, and improves generalizability. This also allows for a more comprehensive performance assessment across various experimental scenarios.

We are also going to release this dataset to the public, and we hope it will serve as a valuable benchmark for assessing approaches in both inverse problems in Physics-Informed Neural Networks (PINNs) and near-field optics.

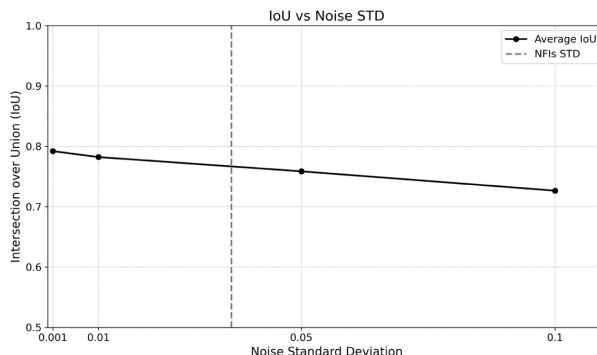


Figure 3: Dependence of IoU on noise level.

6 EXPERIMENTS

In this section, we present the details of our experiments and discuss the results. The optimization process was based on the Lippmann-Schwinger (LS) formalism (see (3), (4)), aiming to optimize the XiEff($\vec{r}; \Theta$) (see (5), (6)) representation from the near-field imaging (NFI) data. The architecture of XiEff was a multilayer perceptron (MLP), similar to the well-adopted architecture in Neural Radiance Field (NeRF) framework Mildenhall et al. (2021); Xie et al. (2022). The XiEff MLP architecture was constant across all experiments, consisting of 9 layers, each with 256 neurons. The MLP accepted a 2-dimensional input corresponding to the spatial coordinates (x, y) , and produced a 4-dimensional output representing the components of the susceptibility tensor \hat{X} . Skip connections were added at the 5-th layer, and positional encoding with a frequency of 7 and a *sin* activation. We

378
 379
 380
 381
 382
 383
 384
 385
 386
 387
 388
 389
 390
 391
 392
 393
 394
 395
 396
 397
 398
 399
 400
 401
 402
 403
 404
 405
 406
 407
 408
 409
 410
 411
 412
 413
 414
 415
 416
 417
 418
 419
 420
 421
 422
 423
 424
 425
 426
 427
 428
 429
 430
 431

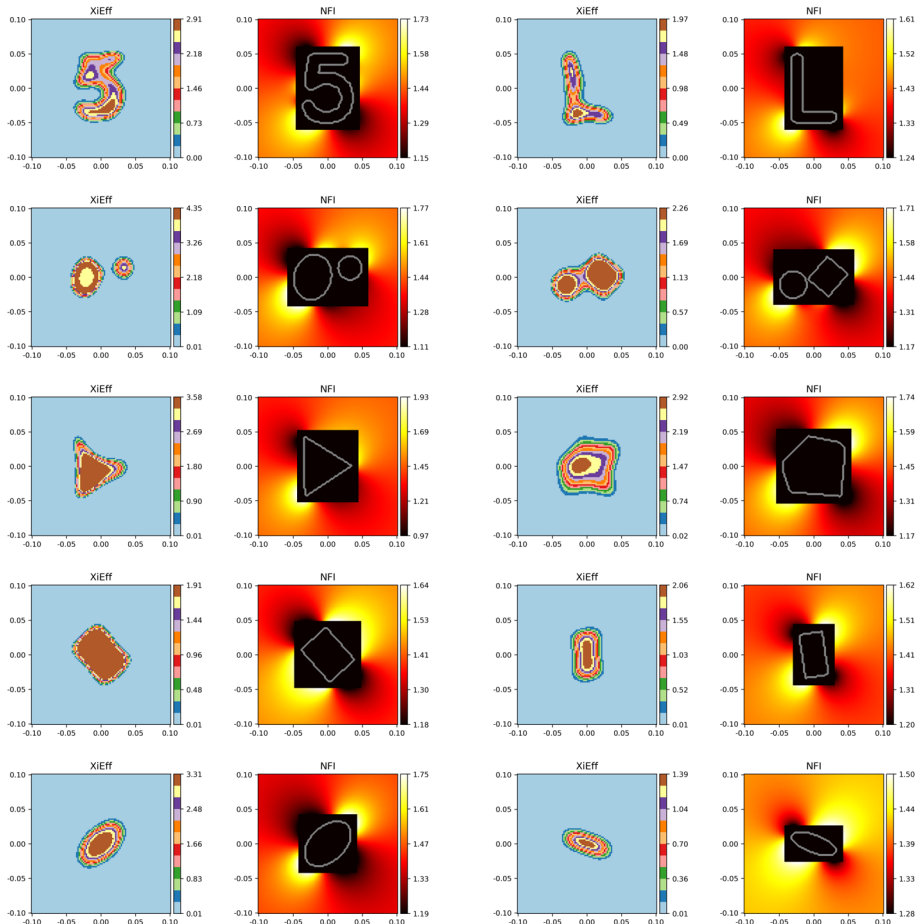


Figure 4: Constant dataset, XiEff and NFI.

employed the Huber loss Huber (1992) as it proved to be more robust than L2 loss. The Huber loss is known to be less sensitive to outliers than the L2 loss, which can be beneficial when dealing with noisy data or observations that may contain some extreme values. Please note that for Θ close to Θ_{optimal} it is basically L2 loss thus lemma from 4.1 is still valid with slight modification.

Regularization was used only during the robustness experiments and was selected to be proportional to the noise level, $\lambda = 0.01 \times \text{STD}(\xi)$. Since XiEff is optimized for each NFI from the dataset and all NFI data is within a batch, we chose to use the second-order L-BFGS algorithm with strong Wolfe conditions Wolfe (1969). Optimization was limited to 20 steps for regular experiments; for robustness measurement experiments we stopped optimization at 10 steps. The entire optimization process for a single NFI (grid 100×100) consumed approximately 1–2 min on 12GB GPU. It is significantly faster than Chen et al. (2020); Chen & Dal Negro (2022) and comparable to Saba et al. (2022). As the quality metric we chose the Intersection over Union (IoU) between the particle shape and the shape of the thresholded norm of XiEff. The IoU is a commonly used metric in computer vision and image segmentation tasks, providing a measure of the overlap between the predicted and ground truth segmentations thus well-suited for the problem under consideration. The threshold for every NFI was chosen to maximize the IoU. In our case, it quantifies the similarity between the optimized XiEff representation and the actual particle shape, enabling us to evaluate the interpretability of the learned representation. The table 1 presents the IoU metrics for both dataset variants with constant and random external fields for each category of shapes: ellipses, rectangles, convex, unions, characters, and the average across the entire dataset.

The IoU values (table 1) showcase the method’s proficiency with simple geometric shapes like ellipses and rectangles, achieving excellent performance across both datasets. For more complex

432
433
434
435
436
437
438
439
440
441
442
443
444
445
446
447
448
449

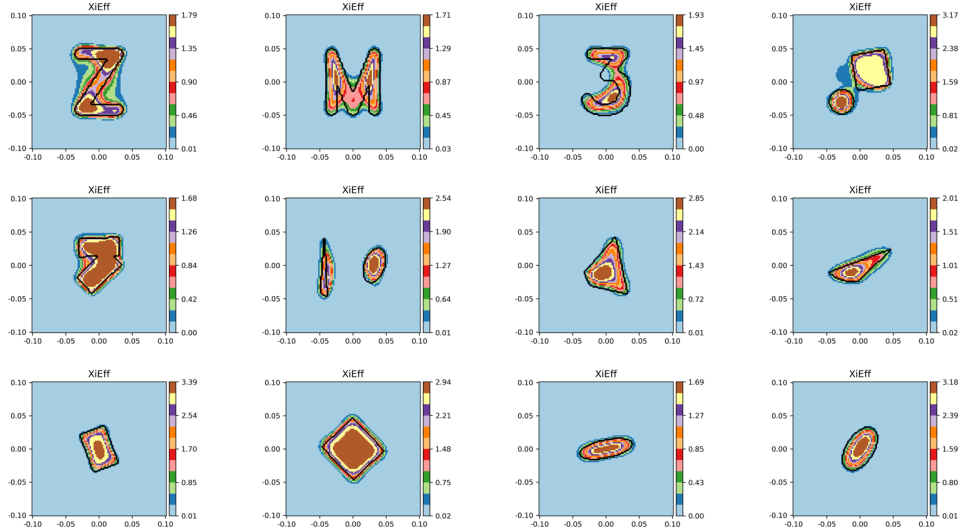


Figure 5: Random dataset: Xieff.

450
451
452
453
454
455
456
457
458
459
460
461
462
463
464

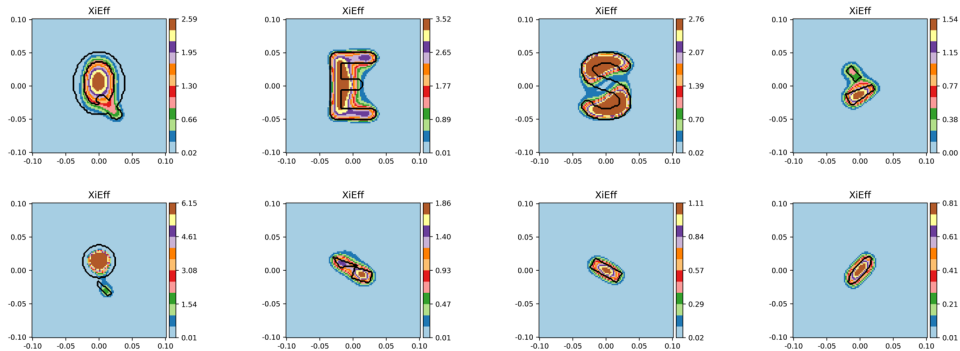


Figure 6: Random dataset: Hard cases.

465
466
467
468
469
470
471
472
473
474
475
476
477
478
479

categories like convex shapes and shape unions, the method still exhibits promising results by faithfully modeling the underlying structure. Overall, the IoU metrics highlight exceptional performance with simple shapes and remarkable generalization to increasing complexities.

Additionally, we conducted experiments regarding robustness to noise. These experiments involved adding Gaussian noise to the NFIs and measuring the IoU for the random variation of the dataset. The results of this modeling are presented in Figure 3, which displays the IoU versus the level of the noise injected. The level of the standard deviation of the NFI within the dataset variation without noise is also displayed. As we can see, the proposed method is robust because the IoU metric degrades slowly, even in cases where the noise level is significantly higher than the standard deviation of the dataset NFIs. This robustness is a crucial property for practical applications, where measurement noise is inevitable, and it demonstrates the effectiveness of the proposed approach in handling noisy observations.

480
481
482
483
484
485

Figure 4 displays the visualization of the constant dataset variant NFI with the corresponding Xieff representation. As you can see, the NFI images of different particles are very similar to one another and are not explainable. However, the corresponding Xieff representation (the result of optimization from the NFI data) is highly similar to the particle shape, providing excellent interpretability for the NFI images. This interpretability is a key advantage of the proposed method, as it enables a better understanding of the underlying physical phenomena and the characteristics of the particles under investigation.

486 The random dataset variant is displayed in Figure 5 with the XiEff representation but without the
487 NFIs due to the low visual clarity of the NFIs with randomly changed external fields at every probe
488 position. As you can see, it works well even for more complex particle shapes, demonstrating the
489 versatility and generalization capabilities of the proposed approach.

490 The method fails in two types of cases (see figure 6): first, thin or small-sized particles, and second,
491 particles with holes. We can assume that the first type of failure case may potentially be partially
492 improved by changing the neural network architecture, optimization process, or even by increasing
493 the level of discretization. However, the second type of failure case cannot be easily resolved due to
494 the physical limitations, as a similar problem exists in classical optics as well. These failure cases
495 highlight the need for further research and improvements, particularly in addressing the limitations
496 posed by complex particle geometries.

499 7 CONCLUSION

502 In this work, we introduced a novel computer vision algorithm—the XiEff representation—that
503 leverages neural fields to model the effective susceptibility tensor in near-field optics. By integrating
504 this representation into the Lippmann-Schwinger integral equation, we developed an unsupervised
505 method to reconstruct the effective susceptibility directly from imaging data, operating without the
506 need for labeled or external data. Also the proposed algorithm is without any method specific hy-
507 perparameters and as result efficient in tuning.

508 Our experimental validation on synthetic data demonstrated high accuracy, with the method per-
509 forming well on both simple and complex shapes and achieving high Intersection over Union (IoU)
510 scores. Theoretical analysis and empirical evaluations confirmed the method’s robustness to mea-
511 surement noise, ensuring reliable convergence even with noisy observations. This robustness is
512 crucial for practical applications where measurement noise is inevitable.

513 Furthermore, we proposed a new scanning strategy for SNOM, where the external field is random-
514 ized at each probe position. Our experiments with this random dataset showed an increase in the
515 quality of the inverse problem solution. This approach appears to be universal and could potentially
516 improve the performance of other inverse algorithms in similar domains.

517 The optimized XiEff representation offers improved interpretability by providing a physically mean-
518 ingsful model directly connected to the optical characteristics of objects. It effectively addresses the
519 limited visual clarity of raw near-field images, which are often challenging for human perception to
520 interpret.

521 In addition, we have developed a comprehensive synthetic dataset that will be publicly released,
522 potentially serving as benchmark for inverse problems in near-field optics and PINNs.

524 Our successful application of an integral equation approach within the PINNs framework is partic-
525 ularly noteworthy, as such cases are relatively rare. This achievement opens new avenues for incor-
526 porating integral equations into physics-informed machine learning, potentially benefiting a wide
527 range of physical problems where integral formulations offer advantages over differential equations.

528 Future research opportunities include exploring more advanced neural network architectures and
529 optimization techniques from the PINNs perspective to further enhance the performance of the XiEff
530 representation. From the near-field optics standpoint, extending the method to three-dimensional
531 geometries, objects on or under surfaces, anisotropic and nonlinear materials, and applying the
532 method to real SNOM data are promising directions. Given that the Lippmann-Schwinger equation
533 is generally valid, the proposed algorithm could be applied to other wave regimes, such as radio
534 frequencies, and could be expanded from the near-field to the far-field zone.

535 In conclusion, our theoretical research, focused on practical outcomes, makes a significant advance-
536 ment in expanding computer vision’s domain into near-field optics modality. The XiEff represen-
537 tation pushes the boundaries of Physics-Informed Computer Vision, demonstrating how interdis-
538 ciplinary approaches can transform scientific imaging, converting complex physical measurements
539 into comprehensible, machine-learned representations which are interpretable from a physical per-
spective.

540
541
542
543
544
545
546
547
548
549
550
551
552
553
554
555
556
557
558
559
560
561
562
563
564
565
566
567
568
569
570
571
572
573
574
575
576
577
578
579
580
581
582
583
584
585
586
587
588
589
590
591
592
593

REFERENCES

- Chayan Banerjee, Kien Nguyen, Clinton Fookes, and Karniadakis George. Physics-informed computer vision: A review and perspectives. *ACM Computing Surveys*, 57(1):1–38, 2024.
- Robert W Boyd, Alexander L Gaeta, and Enno Giese. Nonlinear optics. In *Springer Handbook of Atomic, Molecular, and Optical Physics*, pp. 1097–1110. Springer, 2008.
- Sergei I Bozhevolnyi, VZ Lozovski, and Yu V Nazarov. Diagram method for exact solution of the problem of scanning near-field microscopy. *Optics and Spectroscopy*, 90:416–425, 2001.
- Yuyao Chen and Luca Dal Negro. Physics-informed neural networks for imaging and parameter retrieval of photonic nanostructures from near-field data. *APL Photonics*, 7(1), 2022.
- Yuyao Chen, Lu Lu, George Em Karniadakis, and Luca Dal Negro. Physics-informed neural networks for inverse problems in nano-optics and metamaterials. *Optics express*, 28(8):11618–11633, 2020.
- U Durig, Dieter W Pohl, and F Rohner. Near-field optical-scanning microscopy. *Journal of applied physics*, 59(10):3318, 1986.
- Christian Girard and Alain Dereux. Near-field optics theories. *Reports on Progress in Physics*, 59(5):657, 1996.
- Christian Girard, Alain Dereux, Olivier JF Martin, and Michel Devel. Generation of optical standing waves around mesoscopic surface structures: scattering and light confinement. *Physical Review B*, 52(4):2889, 1995.
- Shudong Huang, Wentao Feng, Chenwei Tang, and Jiancheng Lv. Partial differential equations meet deep neural networks: A survey. *arXiv preprint arXiv:2211.05567*, 2022.
- Peter J Huber. Robust estimation of a location parameter. In *Breakthroughs in statistics: Methodology and distribution*, pp. 492–518. Springer, 1992.
- John David Jackson. *Classical electrodynamics*. John Wiley & Sons, 2012.
- Lev Davidovich Landau, John Stewart Bell, MJ Kearsley, LP Pitaevskii, EM Lifshitz, and JB Sykes. *Electrodynamics of continuous media*, volume 8. elsevier, 2013.
- Xuan Li, Yi-Ling Qiao, Peter Yichen Chen, Krishna Murthy Jatavallabhula, Ming Lin, Chenfanfu Jiang, and Chuang Gan. Pac-nerf: Physics augmented continuum neural radiance fields for geometry-agnostic system identification. *arXiv preprint arXiv:2303.05512*, 2023.
- Valeri Lozovski. The effective susceptibility concept in the electrodynamics of nano-systems. *Journal of Computational and Theoretical Nanoscience*, 7(10):2077–2093, 2010.
- Olivier JF Martin, Alain Dereux, and Christian Girard. Iterative scheme for computing exactly the total field propagating in dielectric structures of arbitrary shape. *JOSA A*, 11(3):1073–1080, 1994.
- Ben Mildenhall, Pratul P Srinivasan, Matthew Tancik, Jonathan T Barron, Ravi Ramamoorthi, and Ren Ng. Nerf: Representing scenes as neural radiance fields for view synthesis. *Communications of the ACM*, 65(1):99–106, 2021.
- Michael Paulus and Oliver JF Martin. Light propagation and scattering in stratified media: a green’s tensor approach. *JOSA A*, 18(4):854–861, 2001.
- Kaare Brandt Petersen, Michael Syskind Pedersen, et al. The matrix cookbook. *Technical University of Denmark*, 7(15):510, 2008.
- Maziar Raissi, Paris Perdikaris, and George E Karniadakis. Physics-informed neural networks: A deep learning framework for solving forward and inverse problems involving nonlinear partial differential equations. *Journal of Computational physics*, 378:686–707, 2019.
- Amirhossein Saba, Carlo Gigli, Ahmed B Ayoub, and Demetri Psaltis. Physics-informed neural networks for diffraction tomography. *Advanced Photonics*, 4(6):066001–066001, 2022.

594 Jia Sun, Yinghua Liu, Yizheng Wang, Zhenhan Yao, and Xiaoping Zheng. Binn: A deep learning
595 approach for computational mechanics problems based on boundary integral equations. *Computer*
596 *Methods in Applied Mechanics and Engineering*, 410:116012, 2023.
597

598 Haixin Wang, Yadi Cao, Zijie Huang, Yuxuan Liu, Peiyan Hu, Xiao Luo, Zezheng Song, Wanjia
599 Zhao, Jilin Liu, Jinan Sun, et al. Recent advances on machine learning for computational fluid
600 dynamics: A survey. *arXiv preprint arXiv:2408.12171*, 2024a.

601 Sifan Wang, Yujun Teng, and Paris Perdikaris. Understanding and mitigating gradient flow patholo-
602 gies in physics-informed neural networks. *SIAM Journal on Scientific Computing*, 43(5):A3055–
603 A3081, 2021.

604 Yizheng Wang, Jinshuai Bai, Zhongya Lin, Qimin Wang, Cosmin Anitescu, Jia Sun, Moham-
605 mad Sadegh Eshaghi, Yuantong Gu, Xi-Qiao Feng, Xiaoying Zhuang, et al. Artificial intelli-
606 gence for partial differential equations in computational mechanics: A review. *arXiv preprint*
607 *arXiv:2410.19843*, 2024b.

608

609 Philip Wolfe. Convergence conditions for ascent methods. *SIAM review*, 11(2):226–235, 1969.

610

611 Yiheng Xie, Towaki Takikawa, Shunsuke Saito, Or Litany, Shiqin Yan, Numair Khan, Federico
612 Tombari, James Tompkin, Vincent Sitzmann, and Srinath Sridhar. Neural fields in visual comput-
613 ing and beyond. In *Computer Graphics Forum*, volume 41, pp. 641–676. Wiley Online Library,
614 2022.

615 Jun-Bo Zhang, Da-Miao Yu, Deng-Feng Wang, and Xiao-Min Pan. Solution of integral equations
616 by physics-informed neural networks for electromagnetic scattering. *Authorea Preprints*, 2024.
617
618
619
620
621
622
623
624
625
626
627
628
629
630
631
632
633
634
635
636
637
638
639
640
641
642
643
644
645
646
647